Received 1 March 2022; | Revised DD Month YYYY; | Accepted 19 November 2018

DOI: xxx/xxxx

ORIGINAL ARTICLE

Calibration of full-disk He I 10 830 Å filtergrams of the Chromospheric Telescope

Zili Shen[1,2] | Andrea Diercke*[1,3] | Carsten Denker[1]

[1]Leibniz-Institut für Astrophysik Potsdam (AIP), Potsdam, Germany
[2]Department of Astronomy, University of Texas at Austin, Texas, USA
[3]Institut für Physik und Astronomie, Universität Potsdam, Potsdam, Germany

Correspondence
*Leibniz-Institut für Astrophysik Potsdam (AIP), An der Sternwarte 16, 14482 Potsdam, Germany, Email: adiercke@aip.de

The Chromospheric Telescope (ChroTel) is a small 10-cm robotic telescope at Observatorio del Teide on Tenerife (Spain), which observes the entire Sun in Hα, Ca II K, and He I 10 830 Å. We present a new calibration method that includes limb-darkening correction, removal of non-uniform filter transmission, and determination of He I Doppler velocities.

Chromospheric full-disk filtergrams are often obtained with Lyot filters, which may display non-uniform transmission causing large-scale intensity variations across the solar disk. Removal of a 2D symmetric limb-darkening function from full-disk images results in a flat background. However, transmission artifacts remain and are even more distinct in these contrast-enhanced images. Zernike polynomials are uniquely appropriate to fit these large-scale intensity variations of the background. The Zernike coefficients show a distinct temporal evolution for ChroTel data, which is likely related to the telescope's alt-azimuth mount that introduces image rotation. In addition, applying this calibration to sets of seven filtergrams that cover the He I triplet facilitates determining chromospheric Doppler velocities. To validate the method, we use three data sets with varying levels of solar activity. The Doppler velocities are benchmarked with respect to co-temporal high-resolution spectroscopic data of the GREGOR Infrared Spectrograph (GRIS). Furthermore, this technique can be applied to ChroTel Hα and Ca II K data. The calibration method for ChroTel filtergrams can be easily adapted to other full-disk data exhibiting unwanted large-scale variations. The spectral region of the He I triplet is a primary choice for high-resolution near-infrared spectropolarimetry. Here, the improved calibration of ChroTel data will provide valuable context data.

KEYWORDS:
Sun: chromosphere; techniques: image processing; methods: data analysis; methods: observational

1 | INTRODUCTION

The Sun has been observed with telescopes for more than 400 years on a regular basis. Long-term observations of sunspots revealed a cyclic behavior of their appearance related to the solar dynamo (Cliver, 2014). Thus, long-term historical sunspot data are still an important part of present science (Diercke, Arlt, & Denker, 2015; Senthamizh Pavai et al., 2016). Nowadays, space observations monitor the Sun continuously with high cadence (tens of seconds) and high-spatial resolution (about one second of arc), e.g., the Solar Dynamic Observatory (SDO, Pesnell, Thompson, & Chamberlin, 2012) with the onboard instruments Atmospheric Imaging Assambly (AIA, Lemen et al., 2012) and Helioseismic

and Magnetic Imager (HMI, Scherrer et al., 2012). In addition to space instruments, full-disk observations from Earth are crucial to understand solar dynamics and activity, e.g., the full-disk Hα λ6562.8 Å observations, which are part of the Global Hα Network (Steinegger et al., 2000). This network initially combined full-disk Hα observations from Big Bear Solar Observatory (BBSO, Denker et al., 1999) in California, Kanzelhöhe Solar Observatory (KSO, Otruba, 1999) in Austria, and Yunnan Astronomical Observatory (YNAO) in China. Today, a total of seven facilities around the Earth monitor the Sun in Hα as part of the network bridging the night gap. Furthermore, the Global Oscillation Network Group (GONG, Harvey et al., 1996) of the U.S. National Solar Observatory (NSO) hosts a similar network. This network consists of six facilities across the globe (Spain, U.S.A., Chile, Australia, and India) with the aim to study the internal structure of the Sun and its dynamics using helioseismology. GONG also provides full-disk Hα observations and magnetograms.

Along with Hα observations, KSO archives include full-disk images of the Sun in the continuum and the Ca II K line core, as well as drawings of sunspots. The Precision Solar Photometric Telescope (PSPT, Coulter, Kuhn, & Lin, 1996) at Mauna Loa Solar Observatory (MLSO) provides full-disk observations in the blue and red continuum, broad-band observations of the Ca II K λ3933.7 Å line, and narrow-band observations in the wings of this line. The Full-Disk Patrol (FDP, Keller, Harvey, & Giampapa, 2003) telescope provides full-disk observations at high-temporal cadence. Besides Hα images, observations in the Ca II K line, in the He I λ10 830 Å triplet, in the continuum, and at other photospheric wavelength positions are possible. Doppler velocity maps can be created as well using the Hα spectral information. The Chromospheric Helium Imaging Photometer (CHIP, Elmore et al., 1998) at Mauna Loa was operated from 1996 until 2013 by the High-Altitude Observatory (HAO). It recorded every 3 min full-disk observations of the Sun at seven wavelength positions around the He I λ10 830 Å.

This study concerns another full-disk imager, i.e., the Chromospheric Telescope (ChroTel, Bethge et al., 2011; Kentischer et al., 2008) on Tenerife, Spain, which is mounted on the terrace of the Vacuum Tower Telescope (VTT, von der Lühe, 1998). It is based on the model of CHIP and also a Lyot filter for He I was provided by HAO. ChroTel is a robotic telescope with an aperture of 10 cm and observes at three different chromospheric wavelengths: Hα λ6562.8 Å, Ca II K λ3933.7 Å, and He I λ10 830 Å. In proximity of the infrared He I line, the instrument is tuned to seven different filter positions around $\pm$3 Å centered on the He I line core. Thus, Doppler maps can be derived based on these filtergrams. The filter positions include the close-by photospheric Si I line and telluric lines. In the regular observing mode of ChroTel, the telescope records every three minutes an image in all three wavelength bands. Higher cadences of up to 10 s are possible in Hα and Ca II K, when continuous data acquisition is limited to a single channel.

Numerous previous studies highlight the importance of the triplet of neutral helium He I λ10 830 Å which originates in the high chromosphere (Kuckein, 2012). It consists of a blue and red component, where the red component is a blend of two lines. The line is a primary choice to analyze the chromospheric magnetic field (see Kuckein, Martínez Pillet, & Centeno, 2012b) and the line-of-sight (LOS) velocities in filaments (see Kuckein, Martínez Pillet, & Centeno, 2012a). In both studies, the authors presented high-resolution spectral observations obtained with the Tenerife Infrared Polarimeter (TIP-II, Collados et al., 2007) at the VTT. A similar study of high-resolution spectroscopy was carried out with the GREGOR Infrared Spectrograph (GRIS, Collados et al., 2012) analyzing LOS velocities of arch filament systems (González Manrique et al., 2018). On the other hand, ChroTel observations were used to to analyze LOS velocities during a flare., which was triggered by a splitting sunspot (Louis et al., 2014). Compared to high-resolution instruments, ChroTel offers a unique advantage of full-disk Dopplergrams in the He I line, which allows us to relate the high-resolution observations with the surrounding structures. Furthermore, full-disk He I Dopplergrams enable us to study large-scale features such as polar crown filaments over several days continuously. Given the wealth of data that ChroTel provides, a method to calibrate the filtergrams and produce full-disk Dopplergrams is necessary to fully exploit this data set.

In the following, we present a method to calibrate the ChroTel He I filtergrams, i.e., the removal of optical aberrations with the help of Zernike polynomials. The calibration is necessary because the filter transmission introduces a non-uniformity in the intensity distribution of each flat-fielded and limb-darkening-corrected filtergram. In Sect. 2, we introduce the ChroTel observations in the He I wavelength band along with the basic pre-calibration steps. In Sect. 3, we describe the method to calibrate the filtergrams yielding a uniform intensity background. In addition, we discuss the derived Doppler velocities from the ChroTel filtergrams and compare them with corresponding Doppler velocities from high-resolution observations of GRIS for a selected sample data set followed by a discussion.

2 | OBSERVATIONS

In the following sections, we introduce the data sets, which we used from ChroTel as well as the data set from the high-resolution spectrograph GRIS, which was used to validate the results derived from the ChroTel observations. Furthermore,

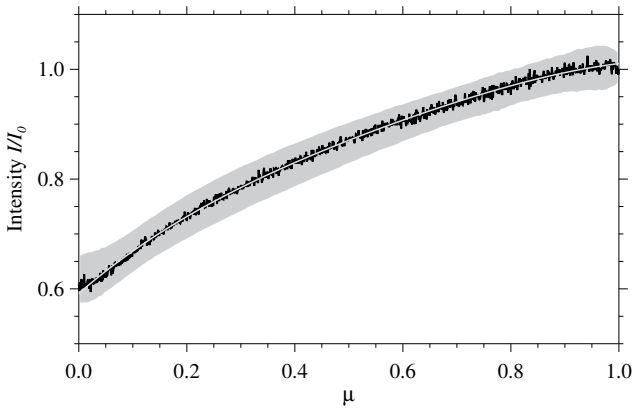

Figure 1 Intensity profile used for the limb-darkening correction of the He I filtergram at 10:09 UT on 2018 March 23. The intensity I/I_0, which was normalized to the quiet-Sun intensity at disk center I_0, is plotted against $\mu = \cos\theta$, where θ is the heliocentric angle. The mean local intensity is plotted in black and the area within three standard deviations of the mean local intensity is shaded in gray. A 4$^{\text{th}}$-order polynomial fit is overplotted as a white curve.

we discuss shortly the ChroTel image quality of the seven filtergrams in He I over the day for one data set.

2.1 | Observations of the Chromospheric Telescope

We selected three data sets of ChroTel with different solar activity levels for the following investigation. Data representing the active Sun was taken on 2014 May 12, whereas low solar activity was encountered during quiet-Sun conditions on 2018 March 23. The data recorded on 2017 June 20 are a good example for typical activity levels.

ChroTel acquires filtergrams at seven wavelength positions in and around the He I triplet (Bethge et al., 2011). The filtergrams are numbered #1 – 7 in order of increasing wavelength, with #4 being the central filtergram. The central wavelengths for the seven filter position are 10 827.45 Å, 10 828.47 Å, 10 829.60 Å, 10 830.30 Å, 10 831.00 Å, 10 832.13 Å, and 10 833.15 Å. Level 1.0 data are available online, which are flat-field corrected and converted to FITS format (Hanisch et al., 2001; Wells, Greisen, & Harten, 1981). Each set of filtergrams in level 1.0 data is ordered with decreasing wavelength. However, we present all results #1 – 7 with increasing wavelength for consistency. The 2048×2048-pixel images are rotated and rescaled so that the radius corresponds to $r = 1000$ pixels, which yields an image scale of about 0.96″ pixel^{-1}. To account for limb-darkening, we derive an average intensity profile for each image, as described in Diercke et al. (2018). The intensity values I for each pixel are plotted against $\mu = \cos\theta$, where θ is the heliocentric angle. The intensity profile is fitted with a 4$^{\text{th}}$-order polynomial

$$I(\mu) = c_0 + c_1 \cdot \mu + c_2 \cdot \mu^2 + c_3 \cdot \mu^3 + c_4 \cdot \mu^4. \quad (1)$$

In the next step, the profile is expanded to a 2D map containing the limb-darkening values for the whole solar disk. After division of the He I filtergrams by the 2D limb-darkening function, dark sunspots and bright areas are removed by masking these region. The 4$^{\text{th}}$-order polynomial fit is then repeated for quiet-Sun regions only. An example of the fitted profile is shown in Fig. 1. The 2D expansion of this profile is again used for the limb-darkening correction of the filtergrams.

2.2 | Observations of GREGOR Infrared Spectrograph

On 2017 June 20, active region NOAA 12663 was observed with GRIS, which is located close to the west limb (Fig. 2). The slit length of GRIS corresponds to 66.3″ with a sampling of 0.136″ pixel^{-1} along the slit. The spectral window covers about 18 Å, which includes the chromospheric He I 10 830 Å line, the Si I, the Ca I, and several telluric lines. The dispersion is about 18 mÅ pixel^{-1}, and the number of spectral points is $N_\lambda = 1010$. The spatial scan was taken from 08:33 UT to 09:00 UT, covering a field-of-view (FOV) of 20″ × 59″. These data will be used in Sect. 3.3 to validate the Doppler velocities derived from ChroTel filtergrams.

2.3 | Image quality

The best image in each data set was identified with the Median Filter-Gradient Similarity (MFGS, Deng et al., 2015) method, which compares the magnitude gradient of the original image to that of its median-filtered counterpart. This metric is implemented in the sTools software package (Denker et al., 2018; Kuckein et al., 2017). The evolution of MFGS values with time over the course of an observing day is shown as an example in Fig. 2 for the data set obtained on 2017 June 20. The best seeing conditions and thus the best images are encountered in the morning for all seven wavelength positions. The central filtergram has a maximum MFGS value of about 0.82 at 08:03:20 UT. The image is visibly sharper compared to the worst central filtergram at 12:18:20 UT with an MFGS value of only 0.76, which appears blurred and unsharp. Increasing turbulence, when the ground is heated by the Sun, and decreasing air mass are competing factors for the prevailing seeing conditions. Thus, mountain-island observatory sites such as Observatorio del Teide experience the best and most stable seeing conditions in the early morning hours. This applies to

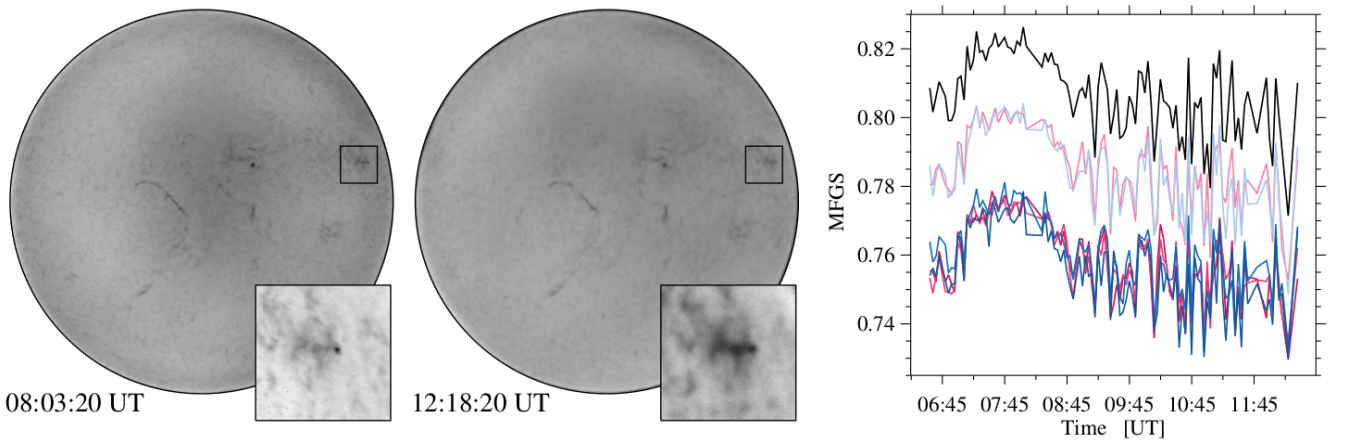

Figure 2 Image quality based on the Median Filter-Gradient Similarity (MFGS) method for the time-series on 2017 June 20. The best (*left*) and worst (*middle*) image of the time-series were recorded at 08:30:20 UT and 12:18:20 UT, respectively. Both images are corrected for limb darkening. Active region NOAA 12663 is marked with a black square and shown enlarged in the lower right corner. Here, the image quality between both images is also visibly different. The MFGS values between 06:33 UT and 12:30 UT (right) were plotted over time for all seven wavelength positions. The black profile represents the central filtergram, and blue and red colors correspond to filtergrams with shorter and longer wavelengths respectively. Lighter shades of blue and red indicate closer proximity to the He I line core. (different). For clarity, the MFGS curves for the central filtergram #4 is shifted up by an offset of +0.1, and the curves for filtergrams #1, #2, #6, and #7 are shifted down by an offset of −0.1.

both synoptic full-disk observations with ChroTel and high-resolution observations with the VTT and the GREGOR solar telescope (Schmidt et al., 2012). Comparing MFGS values of filtergrams at different wavelength positions, the central filtergram reaches highest values (see black profile in the right panel of Fig. 2). The blue and red line-wing filtergrams (light blue and red profiles) exhibit the next highest MFGS values. The lowest values are encountered in the far line-wing and continuum filtergrams. The drop of MFGS values with distance from the He I line core can be explained by the diminishing fine-structure contents of the filtergrams, i.e., the MFGS method is structure dependent, which has to be considered when comparing different types of images. Nonetheless, all MFGS time profiles are tightly correlated with correlation values between 0.89 and 0.95 and display the same trend, i.e., improving seeing conditions until about 08:00 UT, followed by a decrease until 09:00 UT. This time interval clearly demonstrates the changing contributions of air mass and (ground-layer) turbulence to the prevailing seeing conditions. After 09:00 UT, larger MFGS variations on shorter time-scales are observed, which are likely linked to local seeing in the vicinity of ChroTel's roof-mounted turret.

3 | METHODS

3.1 | Zernike polynomials

The limb-darkening corrected filtergrams in Fig. 2 exhibit an uneven background, which is likely introduced by time-dependent filter transmission and image rotation caused by the alt-azimuthal mount of the turret system. The central part of the image is darker with a brighter ring surrounding it. The uneven background is visible in each filtergram and persists throughout the time-series but continuously changes its appearance. These intensity changes across the solar disk and from filtergram to filtergram hamper any efforts to reliably calculate Doppler velocities.

To remedy this shortcoming, we developed a calibration process for ChroTel He I filtergrams using Zernike polynomials to characterize this uneven background. Zernike polynomials are a sequence of orthogonal polynomials on the unit disk, which can be expressed in polar coordinates as a product of angular and radial functions. They are widely used to describe aberrations of optical systems. Since they are orthogonal, Zernike polynomials are often chosen as a basis to represent properties of a circular image with no redundancy. In the following, we will show that Zernike polynomials are well-suited to remove artifacts from solar full-disk images – with applications well beyond the ChroTel data at hand.

Noll (1976) modified the polynomials with a special normalization scheme and introduced a new index system. The

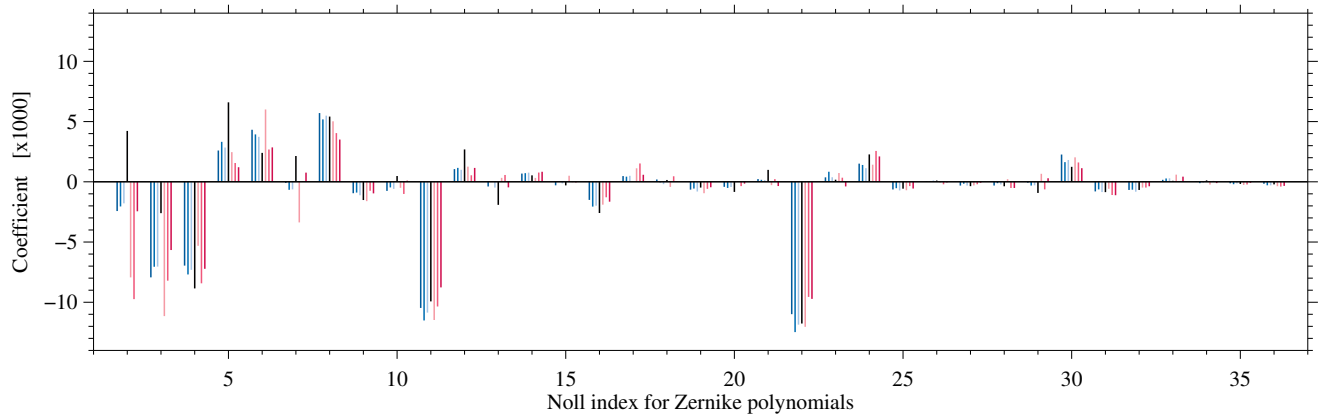

Figure 3 Coefficients of 36 Zernike polynomials fitted to He I filtergrams at seven wavelength positions for the best quiet-Sun data set on 2018 March 23. For each position, the coefficients are displayed in increasing wavelength from left to right. Black refers to the line-core filtergram, while blue and red correspond to the red and blue line wings (see color-coding in Fig. 2).

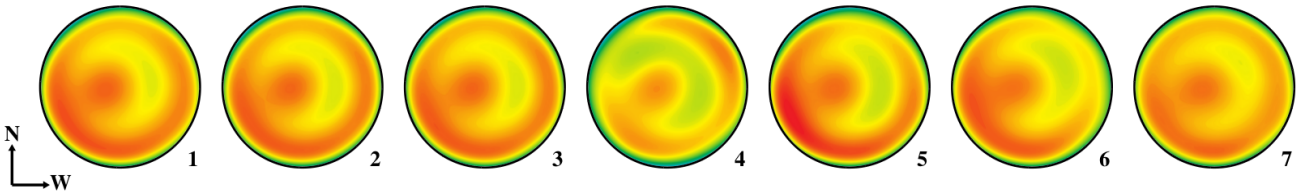

Figure 4 2D reconstruction of the background based on the Zernike coefficients depicted in Fig. 3 for the best quiet-Sun data set on 2018 March 23. Each filtergram is labeled #1 – 7 according to increasing wavelength. The images are scaled in the same interval [0.75, 1.07].

mode-ordering number j is a function of the radial degree n and azimuthal frequency m. The filter transmission is expressed in terms of Zernike polynomials up to mode-ordering number $j = 36$, which corresponds to radial degrees $n \leq 8$ and azimuthal frequencies $|m| \leq 8$.

3.2 | Calibration process

Since the solar radius in ChroTel filtergrams is rescaled to 1000 pixels, we inscribe the circular Zernike polynomials in a square image with 2000×2000 pixels. Zernike polynomials are generated with routines written in the Interactive Data Language (IDL) included in the sTools software repository, which were originally developed by Denker & Tritschler (2005) for measuring the quality of Fabry-Pérot etalons. Fitting arbitrary intensity distributions across a disk, like those of ChroTel He I filtergrams, is also implemented in these IDL routines. Since the geometry of Zernike polynomials matches that of the solar disk in He I filtergrams, the pixel-to-pixel correspondence can be exploited. The intensity values of the limb-darkening-corrected filtergrams are placed in a column vector b with about 3.14×10^6 elements. Similarly, the first 36 Zernike polynomials form the 36 columns, with 3.14×10^6 elements each, of the matrix A. The intensity values in the solar disk are then fitted with a linear combination of 36 Zernike polynomials, which becomes a linear least-squares problem $A \cdot x = b$ using matrix-vector multiplication. Finally, singular value decomposition (SVD, Press et al., 2002) and back-substitution is used to obtain the 36 coefficients x of the Zernike polynomial fit. This calibration has one caveat because it applies only to quiet-Sun regions, where He I absorption profiles are not present. Consequently, active regions and filaments with strong He I absorption features have to be excluded from the fitting procedure. This can be accomplished by masking these regions in He I line-core filtergrams using intensity thresholds and morphological image processing. This process is carried out in three steps. First, the background is computed, including the active regions and filaments, and removed from the line-core filtergram. Second, the corrected filtergram is used to determine the mask for active regions and filtergrams. Third,

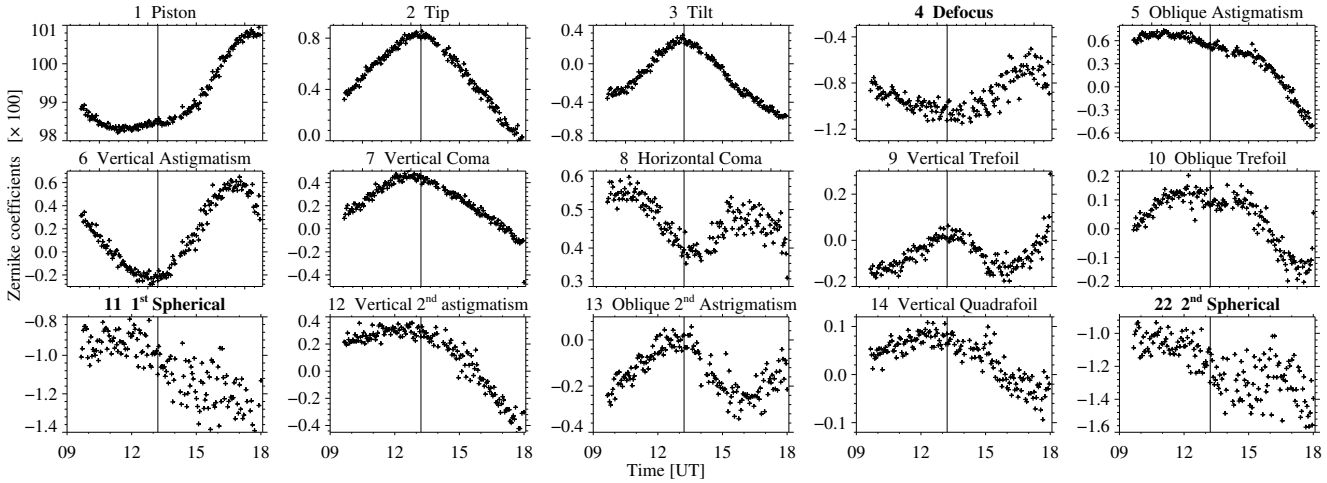

Figure 5 Temporal evolution of Zernike coefficients corresponding to the He I line-core filtergram. The images were taken from 09:39 UT to 17:57 UT on 2018 March 23. Noon local time at the Observatorio del Teide on Tenerife is marked with a vertical line. The title on each panel includes the Noll index j followed by the names of the corresponding optical aberrations. The radial polynomials $j = 4$, 11, and 22 are marked in bold.

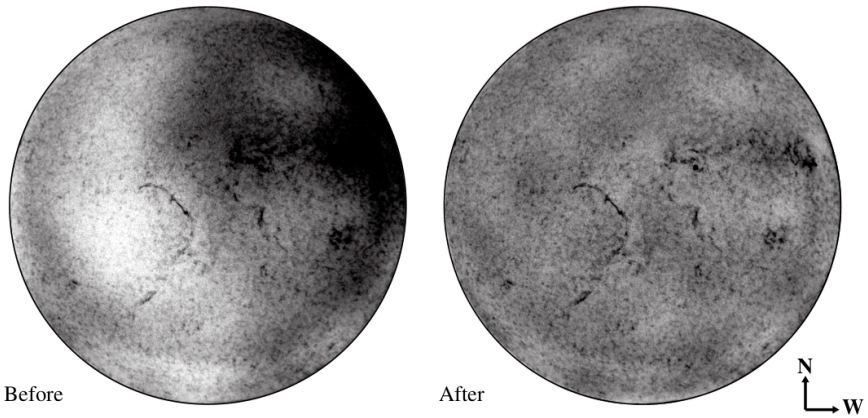

Figure 6 Comparison of a ChroTel filtergram before (*left*) and after (*right*) calibration using the Zernike reconstruction of the background. The He I filtergram was taken in the red line wing (#5) at 08:03:20 UT on 2017 June 20 at a time of average solar activity.

the background is computed excluding active regions and filaments. The mask determined in the second step is applied to all filtergrams at the seven wavelength positions.

To determine the optimal number of Zernike polynomials to be used in the fit, we tested the calibration method on the best quiet-Sun filtergrams which was taken at 10:09 UT on 2018 March 23. On this day, no active regions or filaments were present and thus all pixels in the solar disk were used in the fitting procedure. Figure 3 displays the coefficients for each Zernike polynomial for the set of seven filtergrams. The piston term $j = 1$, representing the average intensity, is not shown. The strongest modes are $j = 4$, 11, and 22. These Zernike polynomials have only a radial component. In optical terminology, $j = 4$ refers to the defocus term, $j = 11$ represents the primary and $j = 22$ the secondary spherical aberration (Noll, 1976). Most sets of the seven Zernike coefficients are similar but not identical for each Noll index j. This points to a common origin for the observed variation of the filter transmission. The variation is sufficient in magnitude to necessitate calibrating the filtergrams individually for each wavelength position. Figure 4 displays the 2D reconstruction of the background using the Zernike coefficients plotted in Fig. 3.

The Zernike reconstructions of the background identify a dark circle near the center and an asymmetrical ring-shaped structure on the disk, both of which correspond to strong radial modes. Attempts to fit more Zernike polynomials reveal higher-order radial modes, while the non-radial polynomials become increasingly smaller. These higher-order polynomials characterize small-scale structures near the edge of the disk or high-frequency radial variations. However, only broad trends across the whole disk are subject of the calibration process.

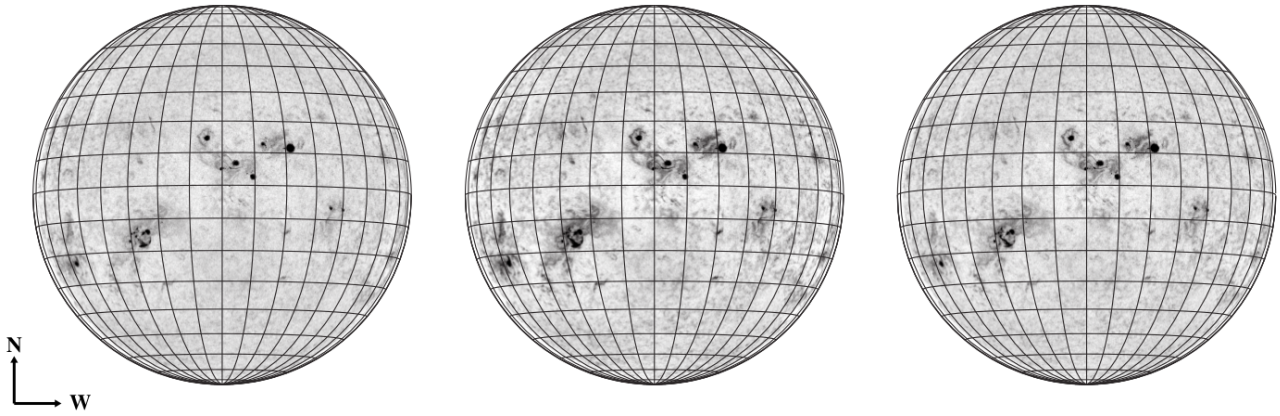

Figure 7 Calibrated ChroTel He I filtergrams taken on 2014 May 12: blue line-wing #3, line-core #4, and red line-wing #5 filtergram (*from left to right*), respectively. The image intensity was scaled in the interval [0.86, 1.03] and a Stonyhurst grid was superposed on the solar disk.

Thus, the limit is appropriately set at $j = 36$, which is also supported by visual inspection of the corrected filtergrams. The orthogonality of Zernike polynomials ensures that the first 36 coefficients will not be affected if higher order terms are neglected. The Zernike fits identify different structures in each filtergram, even though similarities prevail on larger scales. Filtergram #4 refers to the core of the He I line, so that the disk has a lower average intensity than the other filtergrams. The filtergrams were taken with tunable Lyot-type filters, which means that the wavelength position of the transmission peak is shifted very rapidly by applying a variable voltage to liquid crystal retarders between the birefringent stages (Bethge, 2010). This may introduce additional changes between filtergrams, which become visible in the Zernike reconstructions of the background.

In addition, we investigated the evolution of the Zernike coefficients, again using the complete quiet-Sun data set on 2018 March 23. Figure 5 shows the time-dependent variation of the first 14 Zernike coefficients, as well as the coefficients of the radial mode $j = 22$. We only display the coefficients for the time-series of the He I line-core filtergrams because they are representative for the other filter positions as well. The three radial modes $j = 4$, 11, and 22 show a large scatter, while the non-radial coefficients exhibit a clear trend as the day progressed. The piston term $j = 1$ characterizes the average intensity of the solar disk, which is close to unity after limb-darkening correction. Most coefficients, e.g. $j = 2$, 3, and 7, peak at local noon. This suggests that either changes in the light level or elevation of the Sun are responsible for the observed time dependence. ChroTel has an alt-azimuth mount that introduces image rotation, which is however corrected as part of the data reduction. The Lyot filter is mounted in the collimated beam, which results in a stationary pupil. More importantly, the two mirrors of the turret introduce linear polarization, which changes over the day. This influences strongly the transmission of the Lyot filter. A time-lapse movie covering the whole observing period reveals that the central dark spot (Fig. 2) moves across the solar disk. The temporal evolution of the coefficients quantitatively describes how transmission artifacts evolve over time. In principle, the time dependence of the Zernike coefficients can be modeled since the shape of the profiles are rather simple. However, analyzing a large sample of daily He I time-series is beyond the scope of this study. Applying the corrections to a single filtergram takes only about 180 s on a modern desktop computer so that processing time-series data is feasible.

To validate the background calibration procedure employing Zernike polynomials, we evaluate the statistical moments of the intensity distributions on the solar disk. Since strong He I absorption features are absent in quiet-Sun filtergrams, the intensity values are expected to have a symmetrical distribution. Skewness, i.e., a measure of the asymmetry of the intenisty distribution, is mainly introduced by variations in filter transmission. We compare the skewness of the best quiet-Sun filtergrams from 2018 March 23 before and after calibration. The calibration reduces the skewness in most filtergrams. Relevant for determining Doppler velocities (see Sect. 3.3) are the blue and red line-wing filtergrams, where the skewness is reduced from $+0.17$ to $+0.12$ and from -0.10 to -0.02, respectively. The variance of the intensity distribution is also reduced for all seven filtergrams. The average variance is 2.1×10^{-4} before and 0.67×10^{-4} after calibration. The intensity distributions of the calibrated filtergrams are visually more symmetrical and the tails of the distribution are more confined. This raises our

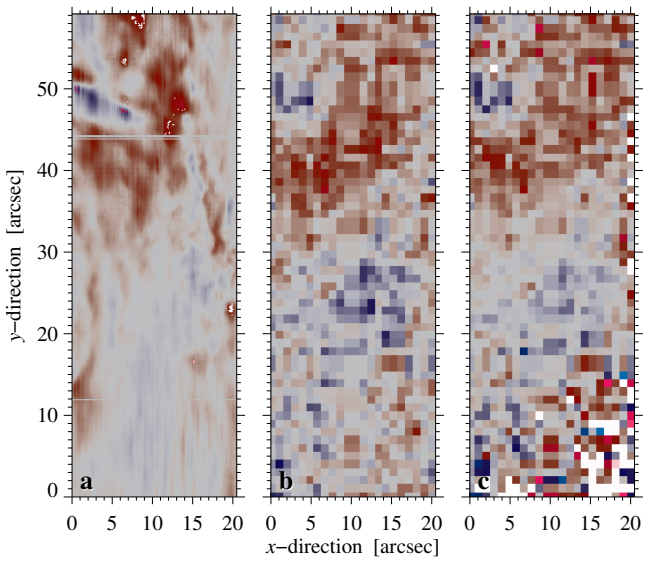

Figure 8 Doppler velocity maps obtained with (a) GRIS and ChroTel, which were derived with (b) the difference method and (c) a parabolic fit to the central three filtergrams. The difference map is scaled between ±0.1 in terms of the normalized quiet-Sun intensity, whereas the other two maps are scaled between ±20 km s^{-1}. The ChroTel maps appear pixelated due to the considerable difference in image scale.

confidence that large-scale variations introduced by the filter transmission were significantly reduced in the filtergrams, resulting in a flat background across the solar disk.

Displaying the calibrated quiet-Sun filtergrams is not very instructive because they are void of any significant absorption structures such as active regions and filaments. Therefore, the best He I red line-wing filtergram on 2017 June 20 was chosen for the direct comparison. Figure 6 clearly demonstrates the improvements after limb-darkening correction and calibration of the background. The intensity was clipped tightly to display the background variations more prominently. The calibration process removed the gradient towards the upper left corner of the image and results in an image with even background. The slightly brighter areas in the center of the solar disk surrounding the active regions are real and were observed in Hα line-wing filtergrams as well (Marquette & Denker, 1999). Finally, the calibrated filtergrams #3 – 5 on 2014 May 12 in Fig. 7 are displayed in a broader intensity range to bring forth details within the active regions. Properly calibrated line-wing and line-core filtergrams are the basis for the derivation of Doppler velocities in the following section.

3.3 | Doppler Velocity

Bethge et al. (2011) produced Doppler maps from ChroTel filtergrams using a center-of-gravity (COG) method to identify the line center. Their COG formula contains arbitrary coefficients to account for filter transmission, blending of different components of the He I line, and other factors that affect real data. These coefficients are optimized for each data set by comparing ChroTel Doppler maps to co-spatial, high-resolution observations of the TIP-II instrument at the VTT. They concluded that for velocities up to about 20 km s^{-1} the inner three filtergrams are sufficient, but the coefficients are not universally applicable. New data sets may require re-calibration with near-infrared spectrographic scans. Because of the scarcity of near-infrared spectrographic data, the synoptic observations from ChroTel cannot be fully exploited. Furthermore, the time dependence of the Zernike coefficients (see Sect. 3.2 and Fig. 5) implies that such a cross-calibration is only valid for a short period of time (tens of minutes).

The calibration of the He I filtergrams with the help of Zernike polynomials allows us to test two methods to derive Doppler velocities. The first method is a simple difference map, where the red line-wing filtergram is subtracted from the blue line-wing filtergram. The second method is a parabolic fit to the "line profile" of the inner three filtergrams. The reference Doppler velocities are obtained with GRIS from a high-resolution spectrograph scan taken on 2017 June 20 between 08:33 UT and 09:00 UT. The scan covers parts of active region NOAA 12663 near the west limb. The Doppler shift map from GRIS is compiled by fitting the He I line core in each pixel with a parabola and determining its minimum position. The corresponding Doppler velocity map is shown in Fig. 8a, scaled between ±20 km s^{-1}.

Multiple ChroTel filtergrams were taken during the scanning period of GRIS, and we chose the filtergram with the best seeing conditions at 08:33 UT for comparison. The GRIS scanning time is around half an hour, shorter than the time scale of the temporal evolution of the Zernike coefficients of about 2–3 hours. The region scanned with GRIS is extracted from the ChroTel filtergrams and carefully aligned to the GRIS map. In addition to the continuum image, the Doppler maps from ChroTel and GRIS are also aligned with respect to each other. Figure 8 compares the GRIS Doppler map to ChroTel velocities determined with the two different methods.

After the calibration, the quiet-Sun intensity in areas with no He I absorption is close to unity. The intensity difference between the blue line-wing filtergram #3 and the red line-wing filtergram #5 is directly related to the line shift because of the normalization across the filtergrams. This normalized intensity difference $\delta I = I_r - I_b$ is proportional to the Doppler velocity $v' = C \cdot \delta I$, which is similar as described in the method of Padinhatteeri, Sridharan, & Sankarasubramanian

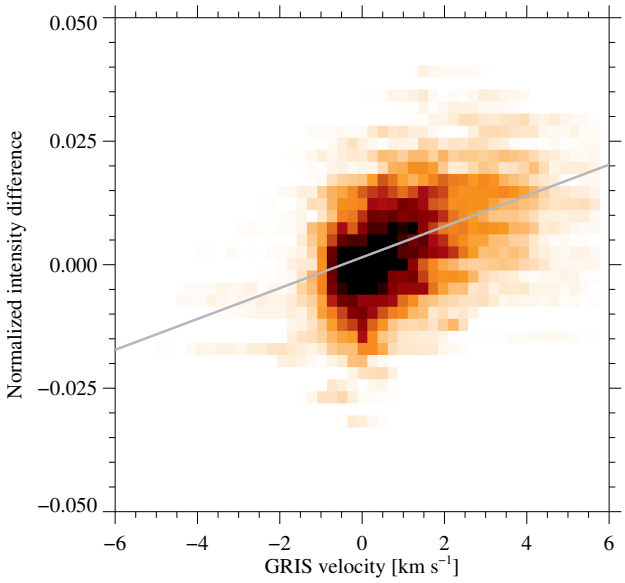

Figure 9 Reference velocity (GRIS) vs. velocity analogue v' (ChroTel). The light grey line depicts a linear regression with a slope of $m = 0.0031$ s km^{-1} and a vertical intercept of 0.0015. The background image is a color-coded 2D histogram.

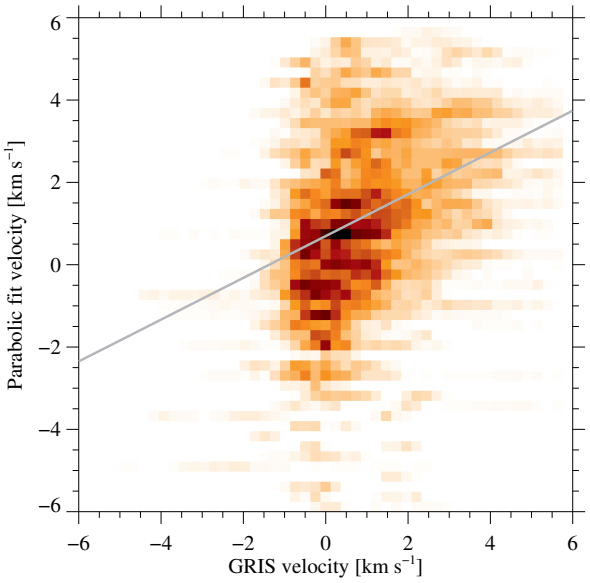

Figure 10 Reference velocity (GRIS) vs. velocity derived with a parabolic fit (ChroTel) in the velocity range of ±6 km s^{-1}. The light grey line depicts a linear regression with a slope of 0.51 and a vertical intercept of 0.70 km s^{-1}. The background image is a color-coded 2D histogram.

(2010). The factor C will be derived from the comparison with the GRIS Doppler velocities and can then be extended to the full-disk data set. The Dopplergrams from the Michalson Doppler Imager (MDI, Scherrer et al., 1995) on board the Solar and Heliospheric Observatory (SoHO, Domingo, Fleck, & Poland, 1995) are produced similarly with a modified difference method using four filtergrams in the wing.

Since the intensity difference is a proxy for line shift, the resulting velocities should be proportional to the reference LOS velocity. This difference map is presented in Fig. 8b, scaled between ±0.1. This normalized intensity difference has the advantage that it is defined across the entire solar disk. In regions without He I absorption, the intensity of both line-wing filtergrams is normalized to unity, and any background artifacts have been removed by the Zernike fitting. Thus, the difference is close to zero as is the Doppler velocity. This is confirmed in the full-disk difference map in Fig. 11. On the other hand, the line shift in regions with He I absorption is due to both differential rotation and the local plasma motion.

For regions with He I absorption, the contribution from differential rotation results in a broad trend across the solar disk. The Zernike polynomials can identify and remove this from the final calibrated filtergram. The caveat is that large active regions with strong absorption are excluded from the Zernike polynomial fit. In addition, co-temporal GRIS scans cover an area too small to determine differential rotation effects. We need to compare the obtained Doppler velocities to other full-disk He I Doppler maps in order to identify whether differential rotation has been removed.

For the second method, the intensity trace of the inner three filtergrams can be treated as a low-resolution line profile for each pixel location. For pixels with He I absorption as determined from the line-core filtergram, a parabolic fit allows us to compute more accurately the line center and thus the Doppler velocity. We have to exclude some pixels with a negative coefficient for the quadratic term, i.e., where the vertex of the parabola is on the top. The resulting map is shown in Fig. 8c, where the excluded pixels are displayed in white. The map is scaled between ±20 km s^{-1}.

The reference map obtained with GRIS is dominated by stronger red-shifted profiles, representing down-streaming flows in the upper part of the Doppler map (Fig. 8a). In the lower part, weaker blue-shifted profiles are encountered, which represent up-streaming flows. The spatial resolution of GRIS is 0.13″ pixel^{-1}, i.e., roughly ten times better than the ChroTel resolution. As expected from the low spatial and spectral resolution, the ChroTel maps lack fine structure compared to the GRIS map and thus appear pixelated in a direct comparison. More importantly, for each ChroTel velocity value, about 100 GRIS measurements are available, representing different physical conditions in the chromosphere. In consequence, a

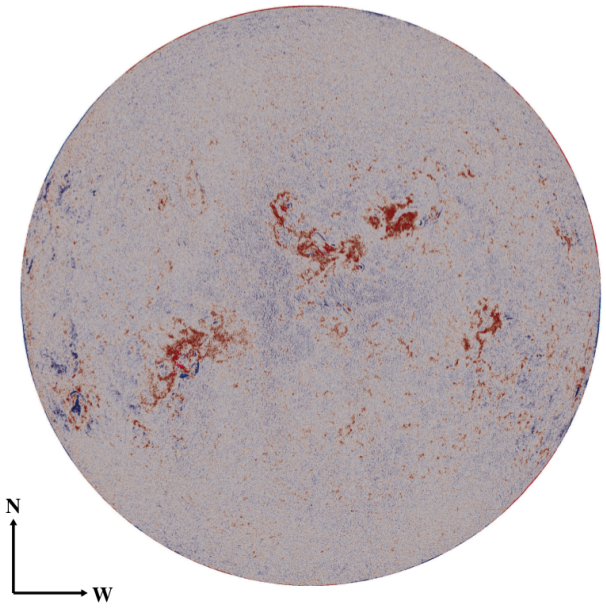

Figure 11 ChroTel full-disk difference maps (red minus blue line-wing filtergram) for the best He I data set on 2014 May 12. The effects of solar differential rotation were removed in the Zernike fitting process. The normalized intensity difference was multiplied by the factor $C = 320\,\mathrm{km\ s^{-1}}$.The images are scaled between $\pm 35\,\mathrm{km\,s^{-1}}$. The median velocities is about $\pm 1.6\,\mathrm{km\,s^{-1}}$ and the velocity outside the active regions is between $\pm 15\,\mathrm{km\,s^{-1}}$.

very tight correlation of the ChroTel and GRIS velocity measurements is not expected. However, the overall structure is recovered in the ChroTel maps, especially in regions with large velocities. Furthermore, the two ChroTel Doppler maps in Fig. 8 are very similar. Next, we will analyze scatter plots of GRIS and ChroTel Doppler velocities for both methods to validate the velocity values in the ChroTel maps.

Figure 9 shows the velocities from the difference map plotted against the reference velocities from the GRIS Doppler map. In the original calibration runs, Bethge et al. (2011) found that reconstructed velocities fall into two regimes: $-5 < v < 5\ \mathrm{km\ s^{-1}}$ and $|v| \geq 5\,\mathrm{km\ s^{-1}}$. In our analysis, we find that a similar separation occurs at $6\,\mathrm{km\ s^{-1}}$. Thus, the following scatter plots will focus on the velocity regime $-6 < v < 6\,\mathrm{km\ s^{-1}}$. From the best linear fit, overplotted in gray, we obtain a slope of $\mathrm{m} = 0.0031\,\mathrm{s\ km^{-1}}$ and a vertical intercept of 0.0015. The factor C determines to $C = 1/m = 320\,\mathrm{km\ s^{-1}}$, which is used to calculate Doppler velocities from the difference map. Linear fits to smaller velocity intervals show the same slope, which indicates that a linear model is appropriate for this relationship. Pearson's linear correlation coefficient between the reconstructed and reference velocities in this regime is $\rho =$ 0.48. In comparison, Bethge et al. (2011) found a correlation coefficient of $\rho = 0.45$ using the central three filters in the $-5 < v < 5\,\mathrm{km\ s^{-1}}$ regime. Thus, a simple difference map with the Zernike-calibrated filtergrams yields comparable results, without resorting to external calibration.

Figure 10 shows the reconstructed velocity from the parabolic fit vs. the GRIS velocity in the $-6 < v < 6\ \mathrm{km\ s^{-1}}$ regime, and the linear fit with a slope of 0.51. The vertical intercept of 0.70 reflects a difference in the rest wavelength. As seen in the scatter plot, the parabolic fit velocities show a larger scatter around the linear trend line, and the correlation coefficient is only $\rho = 0.27$. In both scatter plots, the horizontal striation is a result of enlarging ChroTel data to match the resolution of GRIS. Each pixel in ChroTel data covers many pixels in GRIS data and consequently a range of GRIS velocities. As a sanity check, we computed the linear correlation between the two types of ChroTel Doppler velocities. The high correlation of $\rho = 0.77$ suggests that these two methods deliver consistent results. Finally, a full-disk Doppler map is displayed in Fig. 11 as an example, which corresponds to the best set of filtergrams on 2014 May 12.

4 | DISCUSSION AND CONCLUSIONS

The difference method is more suitable for producing full-disk maps than the parabolic fit method. In regions with low or no He I absorption, spectral line fitting is not an option. In our sample data sets, the parabolic fit is only possible in regions with strong He I absorption, i.e., active regions and filaments. Thus, full-disk Doppler maps are produced with the difference method. We present the parabolic fits for active-region data mainly as a cross check for the consistency of the results. Compared to the COG method provided in the original work of Bethge et al. (2011), the difference map from Zernike-calibrated filtergrams does not require each time an external calibration with a co-temporal spectrograph scan.

Re-calibrating the entire ChroTel archive requires considerable computational resources. In the Zernike calibration procedure, the most computationally intensive part is performing a singular value decomposition on each image. Therefore, modeling the long-term temporal evolution of the Zernike coefficients could minimize computation time. It is possible to avoid repeated fitting procedures if the daily and annual variations of the coeffients can be modeled.

With this new method, ChroTel dopplergrams will no longer be limited by the availability of high-resolution spectrographic data to calibrate the data. Using this method, we are able to produce synoptic maps with ChroTel He I filtergrams as shown in Fig. 12. It uniformly re-normalizes all filtergrams across different days. Synoptic ChroTel data allows studies of solar cycle

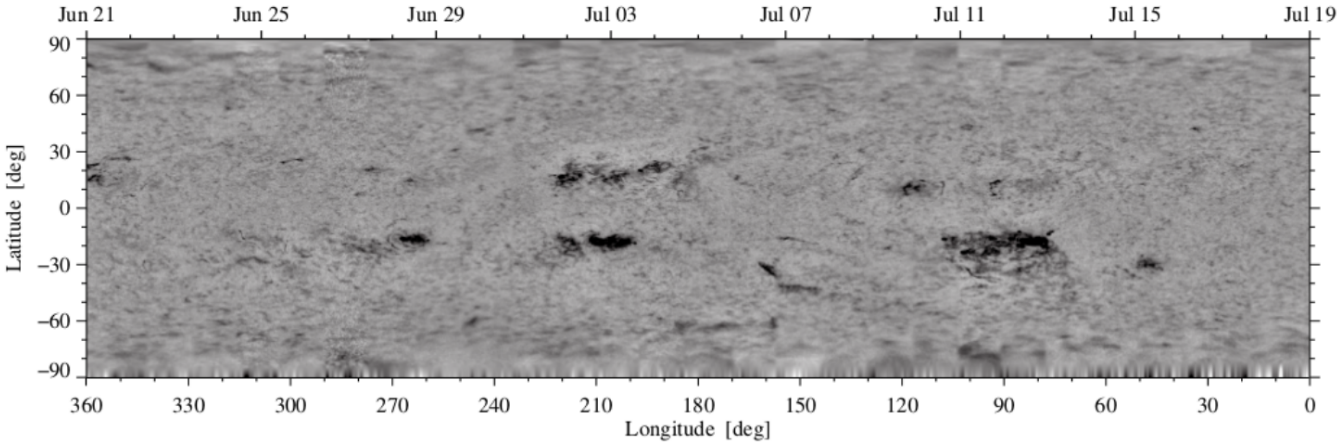

Figure 12 Carrington map (rotation No. 2125) derived from calibrated ChroTel He I line-core images covering the time period from 2012 June 21 to end of July 18. The Carrington map comprises one calibrated full-disk image per day, which was derotated to the respective Carrington latitude with a sampling of 0.1°.

variations and for solar activity monitoring. Solar features can be identified with digital image processing in ChroTel filtergrams. The same method can be employed to reduce the Hα and Ca II K data from ChroTel. In addition, the high-resolution observations of GRIS and other high-resolution spectrographs can be embedded in the large-scale context with full-disk He I filtergrams and Doppler maps. The ChroTel data complements SDO data with data in three chromospheric wavelength.

The calibration method developed in this paper can potentially be applied to other full-disk images. As an example, images from the the Narrowband Filter Imager (NFI) on board the Hinode Solar Optical Telescope (Tsuneta et al., 2008) contain artifacts which are caused by air bubbles in the fluid inside the tunable filter. They distort and move when the filter is tuned, and then usually drift toward the edges of the field of view over time (Tsuneta et al., 2008). Zernike polynomials may be appropriate to model these image artifacts and remove them. Similarly, the Zernike method can be used to characterize background trends and optical artifacts in other solar full-disk images.

ACKNOWLEDGMENTS

ChroTel is operated by the Kiepenheuer Institute for Solar Physics (KIS) in Freiburg, Germany, at the Spanish Observatorio del Teide on Tenerife (Spain). The ChroTel filtergraph was developed by the Kiepenheuer Institute in cooperation with the High Altitude Observatory (HAO) in Boulder, Colorado. ZS's research internship in Germany was made possible by the Research Internships in Science and Engineering (RISE) program of the German Academic Exchange Service (DAAD). CD acknowledges support by grant DE 787/5-1 of the German Research Foundation (DFG). The authors thank Drs. C. Bethge and W. Schmidt for carefully reading the manuscript and helpful comments.

REFERENCES

Bethge, C. 2010. Investigation of large scale structures in the solar chromosphere with the full-disk telescope ChroTel (Unpublished doctoral dissertation). Albert-Ludwigs-Universität Freiburg.

Bethge, C., Peter, H., Kentischer, T. J., Halbgewachs, C., Elmore, D. F., & Beck, C. 2011, October, *A&A*, *534*, A105. doi:

Cliver, E. W. 2014, December, *SSR*, *186*, 169-189. doi:

Collados, M., Lagg, A., Díaz Garcí A, J. J., Hernández Suárez, E., López López, R., Páez Mañá, E., & Solanki, S. K. 2007, May, Tenerife Infrared Polarimeter II. P. Heinzel, I. Dorotovič, & R. J. Rutten (Eds.), The Physics of Chromospheric Plasmas Vol. 368, p. 611.

Collados, M., López, R., Páez, E. et al. 2012, November, *Astron. Nachr.*, *333*, 872-879. doi:

Coulter, R. L., Kuhn, J. R., & Lin, H. 1996, May, The Precision Solar Photometric Telescopes. Am. Astron. Soc. Meet. Abstr. Vol. 188, p. 56.04.

Deng, H., Zhang, D., Wang, T. et al. 2015, April, *SoPh*, *290*, 1479-1489. doi:

Denker, C., Dineva, E., Balthasar, H., Verma, M., Kuckein, C., Diercke, A., & González Manrique, S. J. 2018, *SoPh*, *5*, 236. doi:

Denker, C., Johannesson, A., Marquette, W., Goode, P. R., Wang, H., & Zirin, H. 1999, January, *SoPh*, *184*, 87-102. doi:

Denker, C., & Tritschler, A. 2005, December, *PASP*, *117*, 1435-1444. doi:

Diercke, A., Arlt, R., & Denker, C. 2015, January, *AN*, *336*, 53-62. doi:

Diercke, A., Kuckein, C., Verma, M., & Denker, C. 2018, *A&A*. (accepted)

Domingo, V., Fleck, B., & Poland, A. I. 1995, December, *SoPh*, *162*, 1-37. doi:

Elmore, D. F., Card, G. L., Chambellan, C. W. et al. 1998, July, *Appl. Opt.*, *37*, 4270-4276. doi:
González Manrique, S. J., Kuckein, C., Collados, M. et al. 2018, September, *A&A*, *617*, A55. doi:
Hanisch, R. J., Farris, A., Greisen, E. W. et al. 2001, *A&A*, *376*, 359-380.
Harvey, J. W., Hill, F., Hubbard, R. P. et al. 1996, May, , *272*, 1284-1286. doi:
Keller, C. U., Harvey, J. W., & Giampapa, M. S. 2003, February, SOLIS: An Innovative Suite of Synoptic Instruments. S. L. Keil & S. V. Avakyan (Eds.), Innovative Telescopes and Instrumentation for Solar Astrophysics Vol. 4853, p. 194-204. doi:
Kentischer, T. J., Bethge, C., Elmore, D. F. et al. 2008, July, ChroTel: A Robotic Telescope to Observe the Chromosphere of the Sun. I. S. McLean & M. M. Casali (Eds.), Ground-based and Airborne Instrumentation for Astronomy II Vol. 7014, p. 701413. doi:
Kuckein, C. 2012. Study of the Magnetic Structure of Active Region Filaments (Unpublished doctoral dissertation). Universidad de La Laguna.
Kuckein, C., Denker, C., Verma, M., Balthasar, H., González Manrique, S. J., Louis, R. E., & Diercke, A. 2017, October, sTools - a Data Reduction Pipeline for the GREGOR Fabry-Pérot Interferometer and the High-resolution Fast Imager at the GREGOR Solar Telescope. B. Schmieder, J.-M. Malherbe, & S. Wu (Eds.), Fine Structure and Dynamics of the Solar Atmosphere Vol. 327, p. 20-24. doi:
Kuckein, C., Martínez Pillet, V., & Centeno, R. 2012a, June, *A&A*, *542*, A112. doi:
Kuckein, C., Martínez Pillet, V., & Centeno, R. 2012b, March, *A&A*, *539*, A131. doi:
Lemen, J. R., Title, A. M., Akin, P. F., D. J.and Boerner et al. 2012, January, *SoPh*, *275*, 17-40. doi:
Louis, R. E., Puschmann, K. G., Kliem, B., Balthasar, H., & Denker, C. 2014, February, *A&A*, *562*, A110. doi:
Marquette, W. H., & Denker, C. 1999, *SoPh*, *186*. (frontispiece) doi:
Noll, R. J. 1976, March, *J. Opt. Soc. Am.*, *66*(3), 207–211. doi:
Otruba, W. 1999, September, High Cadence Digital Full Disk Hα Patrol Device at Kanzelhöhe. B. Schmieder, A. Hofmann, & J. Staude (Eds.), Third Advances in Solar Physics Euroconference: Magnetic Fields and Oscillations Vol. 184, p. 314-318.
Padinhatteeri, S., Sridharan, R., & Sankarasubramanian, K. 2010, September, *sp*, *266*, 195-207. doi:
Pesnell, W. D., Thompson, B. J., & Chamberlin, P. C. 2012, January, *SoPh*, *275*, 3-15. doi:
Press, W. H., Teukolsky, S. A., Vetterling, W. T., & Flannery, B. P. 2002, Numerical Recipes in C++: The Art of Scientific Computing (2nd ed.,). Cambridge, UK: Cambridge University Press.
Scherrer, P. H., Bogart, R. S., Bush, R. I. et al. 1995, December, *SoPh*, *162*, 129-188. doi:
Scherrer, P. H., Schou, J., Bush, R. I. et al. 2012, January, *SoPh*, *275*, 207-227. doi:
Schmidt, W., von der Lühe, O., Volkmer, R. et al. 2012, November, *AN*, *333*, 796-809. doi:
Senthamizh Pavai, V., Arlt, R., Diercke, A., Denker, C., & Vaquero, J. M. 2016, October, *Adv. Space Res.*, *58*, 1468-1474. doi:
Steinegger, M., Denker, C., Goode, P. R. et al. 2000, The New Global High-Resolution Hα Network: First Observations and First Results. A. Wilson (Ed.), The Solar Cycle and Terrestrial Climate, Solar and Space Weather Vol. 463, p. 617.
Tsuneta, S., Ichimoto, K., Katsukawa, Y. et al. 2008, June, *SoPh*, *249*, 167-196.
von der Lühe, O. 1998, November, *New Astron. Rev.*, *42*, 493-497. doi:
Wells, D. C., Greisen, E. W., & Harten, R. H. 1981, *A&AS*, *44*, 363-370.

How cite this article: Z. Shen, A. Diercke, and C. Denker (2018), Calibration of full-disk He I 10 830 Å filtergrams of the Chromospheric Telescope, *Astron. Nachr./AN.*, *????*.

How cite this article: Z. Shen, A. Diercke, and C. Denker (2018), Calibration of full-disk He I 10 830 Å filtergrams of the Chromospheric Telescope, *Astron. Nachr./AN.*, *????*.